In-situ Raman Study on Electrochemical Lithium Insertion into Multi-walled Carbon Nanotubes: The Role of Defects and Crystallization

Yoong Ahm Kim*, M. Kojima, Hiroyuki Muramatsu, Daisuke Shimamoto, Takuya Hayashi and Morinobu Endo
Faculty of Engineering, Shinshu University, 4-17-1 Wakasato, Nagano-shi 380-8553, Japan

Mauricio Terrones
Advanced Materials Department, IPICYT, Camino a la Presa San José 2055,
San Luis Potosí 78216, México

Mildred S. Dresselhaus
Massachusetts Institute of Technology, Cambridge, MA 02139-4307, USA

We have carried out *in-situ* Raman studies during the electrochemical insertion of lithium ions (Li^+) into pristine and thermally treated multi-walled carbon nanotubes (MWNTs). We found an improved structural integrity as well as the removal of defects in the thermally treated tubes. The different Li^+ insertion behaviors above 0.5 V in as-grown and thermally treated tubes could be explained by the presence of defects on the outer surface of the tubes. No changes of Raman spectra from 2.8 to 0.8 V is characterized by the coverage of Li^+ on the outer surface of tubes whereas the upshift of G band and the absence of a separated G band below 0.75 V indicate the formation of diluted graphite intercalation below stage 2 phase (LiC_{12}).

KEYWORDS: Raman spectroscopy; Carbon Nanotubes; Annealing; Defects; Lithium ion.

*Correspondence to: Yoong Ahm Kim, Faculty of Engineering, Shinshu University, 4-17-1 Wakasato, Nagano, Japan. E-mail: yak@endomoribu.shinshu-u.ac.jp

INTRODUCTION

Carbon structures are now widely used as anode materials in order to overcome safety problems related to lithium ion secondary batteries (LIBs). Therefore, several types of carbon materials exhibiting different morphologies and textures have been widely investigated so as to fabricate high energy and power density Li^+ batteries. At present, more electronic devices are becoming portable and therefore LIBs are an excellent option to achieve good performance and lightweight. More recently, researchers have reported that LIBs could be used in hybrid vehicles with an upgraded high performance (e.g., a large capacity, good rate capability and long cycle life). In this context, carbon nanotubes (single- and multi-walled carbon nanotubes, SWCNTs and MWCNTs) have been evaluated as an efficient electrode material because they are able to store a large amount of Li^+ reversibly.[1-6] Some commercialized LIBs have now incorporated carbon nanotubes as an efficient filler to extend their lifetime.[7,8] However, the contradictory Li^+ intercalation behaviors in MWCNTs such as intercalation/de-intercalation and doping/de-doping[9, 10] can be explained by highly different diameters and structural integrities (e.g., the amount of defects) of carbon nanotubes.

In this study, we selected *in-situ* Raman spectroscopy coupled with an electrochemical system in order to gain more detailed understanding related to the Li^+ insertion and removal within catalytically grown thin carbon nanotubes exhibiting different degrees of crystallinity.[9-13] It is demonstrated that both pristine and thermally treated thin tubes store Li^+ via both doping through defects on the outer surface as well as the formation of dilute intercalation compounds in the inter-shell spacing of the tubes.

EXPERIMENTAL

Catalytically grown carbon nanotubes with a diameter of 20 nm were purchased from the Iljin Company (Korea). The thermal annealing experiments were carried out at various temperatures ranging from 1500 to 2800 ^oC in an argon atmosphere using a graphite furnace. These heat treatments are expected to alter significantly the local structure of nanotubes by removing the defects and the subsequent evaporation of metallic species contained within the nanotube cores.

Scanning electron microscope studies (SEM, JEOL JSM-6335Fs) and transmission electron microscopy (TEM, JEOL JEM-2010FEF, 200 kV) were carried out in order to characterize the macro-morphology and micro-texture of the pristine and thermally treated tubes. Raman spectra were collected using a Kaiser HoloLab 5000 system with an excitation source of 532 nm obtained with a Nd:Yag laser line. X-ray powder diffraction measurements (JEOL-JDX3532, CuK_α (λ=1.54056 Å)) were employed to monitor the overall crystallinity changes.

Finally, the electrochemical measurements were performed using a 2032 button coin cell (Hohsen Corp.). In particular, a homogeneous paste was obtained by mixing carbon nanotubes at 90 wt %

with poly(vinylidene fluoride) at 10 wt % using 1-methyl -2-pyrrolidinone as a solvent. Subsequently, the working electrodes were prepared by attaching the carbon paste onto a nickel mesh (5 mm × 5 mm, purity 99 %) and pressed them together at a pressure of 4903 kPa. The working electrode and separator (thickness = 30 μm), cap, spring, spacer, gasket and cases were placed in a vacuum oven at 100 ^{o}C for 20hrs. A lithium metal sheet (thickness = ca. 0.6 mm) was used as a counter electrode. The electrolyte used in this study consisted of 1M solution of $LiClO_4$ dissolved in a 50:50 mixture by volume of ethylene carbonate (EC) and diethyl carbonate (DEC). Once the cell was assembled in the right order, it was sealed with an insulating clipper in a glove-box. The specific capacity of the nanotube foils was measured by a potentiostat/galvanostat (Nagano Co., Ltd., BTS2004W) during the charge and discharge cycles in the ranges of 0 and 2.8 V, with a current density of 30 mA/g-carbon. During the charge and discharge processes, *in-situ* Raman studies (Kaiser HoloLab5000 system: 532 nm Ar-ion laser line) were carried out by setting the microprobe (× 50, spot size of 1.5 μm) of the microscope at the observation hole of the coin cell.

RESULTS AND DISCUSSION

Relatively long but distorted (not straight) nanotubes were severely entangled to form aggregates (Fig. 1 (a, b)); a typical morphology observed in nanotubes produced using the chemical vapor deposition (CVD) method in the presence of a metal catalyst. Catalytically grown carbon nanotubes have been considered to be structurally defective due to their low formation temperature (< 1000 ^{o}C) as compared to arc-discharge grown nanotubes (ca. 4000 K). Therefore, we performed thermal treatment experiments under an argon atmosphere, to intentionally remove a large portion of defects and the incorporated metallic compounds.[14-16] When the pristine tubes were thermally annealed at 2800^{o}C, there were no significant changes in the overall macro-morphology (see Fig. 1). In order to visualize the changes induced by the heat treatments, we have carried out detailed high resolution transmission electron microscopy (HRTEM) studies on the different nanotube materials. From low-resolution TEM images (see Fig. 2 (a)), the pristine tubes appeared always curled and bent, exhibiting diameters ranging from 20 to 30nm. In general, pristine tubes were coated with less crystalline carbon materials, and in some cases partially aligned carbon materials were observed attached to the inner nanotube layers (possibly catalytically precipitated carbon; Fig. 2 (b)). Interestingly, these tubes possess relatively round cross-sections (see inset in Fig. 2 (b)). It seems quite difficult to avoid the formation of non graphitic carbons in the pyrolytic process with nanotubes produced in a large scale. Even though it is shown that post preparation treatments (e.g., air oxidation and strong acid treatment) could be one way to remove amorphous carbon selectively.[17] However, these techniques appear not to be applicable to a large-scale production due to their difficulties

in reproducibility. Fortunately, thermal annealing is an effective physical method for enhancing the crystallinity of carbon nanotubes, and this technique has been adopted industrially, and is also able to remove toxic metallic impurities.[14-16] In addition, when considering their fabrication into conducting polymer or ceramic nanotube composites, the high degree of crystallinity of the outermost shell within MWCNTs is very important because electrical transport occurs mainly on the nanotube surface.[18,19] For example, when treating pristine tubes at 1500^{o}C (see Fig. 2 (c)), it is possible to observe highly crystalline tubes displaying continuous graphene layers along the tubes axes (inset in Fig. 2 (c)). We also noted that for higher thermal treatment temperatures, single tubes start to exhibit a straighter morphology over a short length range (Fig. 2 (d), (h) and (i)), but they are still distorted over a long length range (see Fig. 2 (e)). In addition, their cross sectional morphology becomes more faceted and less round (Fig. 2 (f) and (g)). This partial faceting phenomenon could be attributed to the local graphitization of the walls due to carbon densification effects.

The structural changes of the different tubes have also been studied by powder X-ray diffraction (Fig. 3 (a)), and Raman spectroscopy (Fig. 3 (b)). High thermal treatment temperature resulted in a continuous up-shift and larger intensities of the (002) diffraction lines, indicating the improved crystallinity of carbon nanotubes (closer to the interlayer spacing of perfect graphite which corresponds to 3.35 Å). Also, it is confirmed that iron oxide phases still appear for the sample heat treated at 1500 ^{o}C, but these peaks start to disappear with higher thermal treatment temperatures. Furthermore, the increased intensity of the (10) lines provides additional evidence for an increased in-plane crystallinity via thermal annealing, whereas the absence of the (101) and (100) lines for samples heat treated at 2800^{o}C, indicates the lack of three-dimensional order among the nested graphene cylinders (e.g. turbostratic-like graphite; see Table 1). Raman spectrometry also provides detailed information related to the structural variations of carbon nanotubes, but mainly on the tubes surface.[20] Figure 3 (b) shows that there is no significant change in the *G* band located at 1582 cm^{-1} (E_{2g2} graphite mode), but the intensities and HWHM (the half width at half-maximum intensity) of the *D* band (a defect-induced mode) centered at 1350 cm^{-1} and the *D'* band located at 1620 cm^{-1} (another defect-induced mode), decrease continuously with increasing heat treatment temperature. This is an indicative of the continuous removal of defects within carbon nanotubes (see Fig. 3 (b) and Table 1).[21, 22] In addition, distinctive changes in the *R* value (I_D/I_G, the intensity of the D band over the intensity of the G band) from 0.848 to 0.552 were observed for the pristine and heat treated sample at 1500 ^{o}C; an observation that is consistent with TEM observations discussed above. Furthermore, the high intensity and symmetry of the G' band (overtone of the D band) at 2700 cm^{-1} for the sample

treated at 2800 ^{o}C, also indicates the lack of 3D stacking order,[23] which caused by the mismatching of the concentric cylinders into an ABAB… stacking configuration.

TGA analysis was used to evaluate the oxidation stability (or chemical reactivity) of pristine and thermally treated tubes. We believe that these defects might act as active sites for up-taking oxygen molecules, thus lowering the oxidation temperature. As shown in Fig. 4, higher treatment temperatures provided higher oxidation resistance due to the reduction of active sites (e.g. defects) on the carbon nanotube walls.

Figure 5 shows voltage profiles of the pristine and thermally treated tubes at 2800^{o}C, respectively. Both samples store Li^+ reversibly (ca. 220 mAh/g) and also exhibit an expected initial irreversible capacity (long plateau at 0.9 V), which is closely related to the electrolyte decomposition and the formation of a solid-electrolyte interface (SEI).[24] Based on a recent study on the extent of the irreversible capacity dependence on the active surface area of carbon materials,[25] thermally treated tubes have to show a short plateau at 0.9 V due to their decreased defect density obtained after thermal annealing. Unexpectedly, and to our surprise both samples show very similar voltage characteristics including the irreversible capacities. Therefore, it is expected that both samples could host Li^+ but the insertion-desertion mechanisms would be different because thermal treatment induces large changes in structural integrity including defect density. Thus, we directly compare voltage profiles of the second cycle for both samples (see Figure 6). Interestingly, Li^+-insertion behavior is very similar but we found that they have different voltage profiles for the charging (Li^+-desertion) process. Mochida *et al.* proposed storage sites for Li^+ in typical soft carbons obtained by thermally treating mesophase pitch at 700 and 1000 ^{o}C, respectively.[26] Similar explanation could be applicable for our samples. For the pristine sample, Li^+ could enter via intercalation and defect. Consequently, in the thermally treated tubes, the Li^+ insertion is expected to be different. Here, we believe that Li^+ could be stored on some defects present on the outer nanotube surface (see D band in Raman spectra), but the relative amount of stored Li^+ in a defect site would be smaller than that of the pristine sample. In addition, the improved interlayer texture by thermal treatment allows Li^+ to accumulate mainly in between graphene layers via intercalation.

The detailed electrochemical Li^+ insertion for types of both samples were then studied using *in-situ* Raman. As a reference sample, we obtained *in-situ* Raman spectra for synthetic graphite (ca. 45 μm, Wako Company) electrodes. In this case, Li^+ intercalation mainly occurs below 0.25 V and three distinct plateaus at 0.18, 0.08 and 0.05 V were observed. The upshift in the G band at 0.15V (Fig. 7) is thought to be due to the random intercalation of Li^+ in a highly dilute state.

Then, the separation of the G bands at 0.075 V, indicates a staging structure (graphite intercalation compounds): G bands at 1600 and 1580 cm^{-1} could be assigned to the graphene layers without and with Li^+ ion intercalates (bounding layer mode).[9] By observing color changes in the observation hole of the coin cell, we could see the intercalation status very clearly. Specifically, the appearance of a light yellow color at the observation hole at 0.05V, provides strong evidence of a stage 2 phase (LiC_{12}). Upon full Li^+ intercalation, we observed a more intense yellow color, corresponding to LiC_6.

Figure 8 depicts *in-situ* Raman spectra as a function of potential for the pristine and thermally treated tubes, respectively. Here we note that both samples exhibit similar Raman spectra through the electrochemical insertion-desertion of Li^+ ions, which is consistent with the voltage profiles observed in Fig. 5. We can divide the changes in the G band upon doping with Li^+ into two regions. The first region is found from 2.8 to 0.8 V and is characterized by the simple coverage of Li+ on the outer surface of pristine and thermally treated tubes. However, the distinctive presence of D' band (around 1620 cm^{-1}) in pristine tubes (Fig. 5 (a)), which is known to originate from the end plane of graphene layers,[27] can be explained by the large density of defects on the outer surface of the tubes. In addition, the depressed D' band intensity with decreasing external voltages seems to be the preferential reaction of Li^+ with defects in pristine samples, because the edge plane is more chemically reactive than the basal plane. Note that the Raman lines at 1452, 1477 and 1788 cm^{-1} correspond to the CH_2 bending modes of the PC solvent molecules.[28] The distinctive upshift in the G band was observed at an applied potential of 0.75 V, followed by the formation of an SEI film. This change is understandable because the dilute intercalate Li^+ might modify the electron density and electrical conductivity of the concentric shells through a charge transfer.[11] Furthermore, the more prominent upshift in the G band for thermally treated samples strongly supports the increased amount of intercalated Li^+ due to their highly developed graphene layers. After fully inserting Li^+ ion into both tubes, the absence of a separated G band and yellow color at the observation hole indicate the formation of diluted graphite intercalation compounds below stage 2 phase (LiC_{12}), which is directly related to the value of the observed reversible capacity for both samples (ca. 220 mAh/g). The fully depressed Raman intensity for both samples at an applied potential of 0.0 V can be explained the abruptly increased electrical conductivity of the electrode. The largely depressed intensity of Raman spectra for fully Li^+ deserted pristine tubes is a strong indication for the large amount of entrapped Li^+ in the defect sites.

CONCLUSIONS

Catalytically grown defective MWCNTs with diameters of 20 nm were thermally treated at various temperatures in the range from 1500 to 2800 ^{o}C in an argon atmosphere, and then their structural changes were analyzed using various techniques. A clear structural enhancement of the degree of the crystallinity within the tubes for thermally treated nanotubes is confirmed from TEM, XRD and Raman studies. To understand the effect of defects on the different electrochemical behaviors of defective and crystalline tubes, we have observed Raman spectra during electrochemical Li^+ insertion/desertion processes for as-produced and thermally treated tubes. No large changes of the G band for both tubes at the external voltages ranging from 2.8 to 0.8 results from the simple coverage of Li^+ on the outer surface of the tubes. However, the largely depressed D' band at 1620 cm^{-1} of as-grown tubes and the irreversibly reduced Raman intensity of the fully Li^+ deserted as-grown tubes provided strong evidence of the presence of defects on the outer surface of the tubes. However, the upshift of G band and the absence of a separated G band below 0.75 V indicate the formation of diluted graphite intercalation below stage 2 phase (LiC_{12}). From our systematic studies, we can conclude that the as-produced defective tubes store Li^+ in both defects and interlayer spacing, but the thermally treated tubes store Li^+ mainly in the interlayer spacing.

Acknowledgements

This work was partially supported by the CLUSTER (the second stage) and a Grant-in-Aid (No.18710084) from the Ministry of Education, Culture, Sports, Science and Technology of Japan. One of the authors (M.S.D.) acknowledges support under NSF/DMR 04-05538. We also thank CONACYT-Mexico for grants: 45772 (M.T.), 41464-Inter American Collaboration (M.T.), the MIT-CONACYT program (M.S.D, M.T.), 2004-01-013-SALUD-CONACYT (M.T.) and PUE-2004-CO2-9 Fondo Mixto de Puebla.

REFERENCES

1. Che GL, Lakshmi BB, Fisher ER, Martin CR. *Nature* 1998; **393**: 346.
2. Leroux F, Metenier K, Gautier S, Frackowiak E, Bonnamy S, Beguin F. *J. Power Sources* 1999; **81**: 317.
3. Gao B, Kleinhammes A, Tang XP, Bower C, Fleming L, Wu Y, Zhou O, *Chem. Phys. Lett.* 1999; **307**: 153.
4. Claye AS, Fischer JE, Huffman CB, Rinzler AG, Smalley RE. *J. Electrochem. Soc.* 2000; **147**: 2845.
5. Shimoda H, Gao B, Tang XP, Kleinhammes A, Fleming L, Wu Y, Zhou O. *Phys. Rev. Lett.* 2000; **88**: 015502.
6. Lu W, Chung DDL. *Carbon* 2001; **39**: 493.
7. Endo M, Kim YA, Hayashi T, Nishimura K, Matushita T, Miyashita K, Dresselhaus MS. Carbon 2001; 39: 1287.
8. Sotowa C, Origi G, Takeuchi M, Takeuchi K, Nishimura Y, Kim YA, Nishikawa D, Hasegawa T, Hayashi T, Endo M, Dresselhaus MS. *The Use of a Combination of Carbon Nanotube and Carbon Black as a Filler to Improve the Cathode Performance of Lithium-ion Batteries*, Submitted to Carbon.
9. Maurin G, Bousquet Ch, Henn F, Bernier P, Almairac R, Simon B. *Solid State Ionics* 2000; **136-137**: 1295.
10. Mi CH, Cao GS, Zhao XB. *J. Electroanalytical Chemistry* 2004; **562**: 217-221.
11. Inaba M, Yoshida H, Ogumi Z, Abe T, Mizutani Y, Asano M. *J. Electrochem. Soc.* 1995; **142**: 20.
12. Inaba M, Yoshida H, Ogumi Z. *J. Electrochem. Soc.* 1996; **143**: 2572.
13. Kim YA, Kojima M, Muramatsu H, Umemoto S, Watanabe T, Yoshida K, Terrones M, Dresselhaus MS. *Small* 2006; **2**: 667.
14. Andrews R, Jacques D, Qian D, Dickey EC. *Carbon* 2001; **39**: 1681.
15. Kim YA, Osada K, Hayashi T, Endo M, Dresselhaus MS. *Chem. Phys. Lett.* 2003; **380**: 319.
16. Kim YA, Hayashi T, Endo M, Kaburagi Y, Tsukada T, Shan J, Osato K, Tsuruoka S. *Carbon* 2005; **43**: 2243.
17. Endo M, Kim YA, Fukai T, Hayashi T, Oshida K, Terrones M, Dresselhaus MS. *Appl. Phys. Lett.* 2002; **80**: 1267.
18. Dai H, Wong EW, Lieber CM. *Science* 1996; **272**: 523.
19. Frank S, Poncharal P, Wang ZL, deHeer WA. *Science* 1998; **280**: 1744.

20. Dresselhaus MS, Dresselhaus G, Saito R, Jorio A. *Physics Reports* 2005; **409**: 47.
21. Andrews R, Jacques D, Qian D, Dickey EC. *Carbon* 2001; **39**: 1681.
22. Chen J, Shan JY, Tsukada T, Munekane F, Kuno A, Matsuo M, Hayashi T, Kim YA, Endo M. *Carbon* 2007; **45**: 274.
23. Kiang CH, Endo M, Ajayan PM, Dresselhaus G, Dresselhaus MS. *Phys. Rev. Let.* 1998; **81**:1869.
24. Besenhard JO, Winter M, Yang J, Biberacher W. *J. Power Sources* 1995; **54**: 228.
25. Béguin F, Chevallier F, Vix-Guterl C, Saadallah S, Bertagna V, Rouzaud JN, Frackowiak E. *Carbon* 2005; **43**: 2160.
26. Mochida I, Ku CH, Yoon SH, Korai Y. *J. Power Sources* 1998; **75**: 214.
27. Katagiri G, Ishida H, Ishitani A. *Carbon* 1988; **26**: 565.
28. Odziemkowski M, Krell M, Irish DE. *J. Electrochem. Sco.* 1992; **139**: 3052.

Figure captions

Figure 1 FE-SEM images of the pristine (a-b) and thermally treated tubes at 2800^{o}C (c-d), at different magnifications.

Figure 2 (a-b) TEM images of the pristine tubes showing their lengths and morphologies. Here the fringes of concentric carbon shells are observed and amorphous-like appears to coat the outer tubes layers. Inset depicts a relatively round cross section observed in the pristine samples; (c) TEM image of thermally-treated tubes at 1500^{o}C, showing that the tubes are crystalline (inset shows the cross section of the annealed sample); (d) TEM image of thermally treated tubes at 2000^{o}C (inset displays the typical nanotube cross section); (e) low resolution TEM image of thermally treated tubes at 2300^{o}C; (f-i) TEM images of thermally treated tubes at 2800^{o}C exhibiting highly developed layers but a partially facetted cross section.

Figure 3 (a) X-ray powder diffraction patterns and (b) Raman spectra of pristine and thermally treated tubes as a function of annealing temperatures. Peaks with * mark are iron carbide.

Figure 4 TGA plots showing the clear variations in weight loss for pristine and thermally treated tubes (1% oxygen and argon gas).

Figure 5 Voltage profiles of (a) a pristine and (b) thermally treated MWCNTs at 2800^{o}C showing the charging and discharging stages.

Figure 6 Direct comparisons of voltage profiles for a pristine and thermally treated tube at 2800^{o}C in the 2nd cycle.

Figure 7 *In-situ* Raman spectra of synthetic graphite for the discharging process (insets are captured photos of the observation hole).

Figure 8 *In-situ* Raman spectra of the (a) pristine and (b) thermally treated MWCNTS at 2800^{o}C for the discharging and charging processes.

Table 1 Structural parameters for pristine and thermally treated multi-walled carbon nanotubes at different temperatures ranging from 1500 to 2800°C.

I. D.	d_{002} [a]	HWHM (cm^{-1}) [b]			$I_{D'}/I_G$ [c]	I_D/I_G [d]	$I_{G'}/I_G$ [e]
		D'-band	G-band	D-band			
Pristine	0.343	24.9	47.8	59.0	0.280	0.848	0.752
HTT1500	0.344	25.7	42.9	54.8	0.209	0.552	0.810
HTT1800	-	21.4	33.2	42.3	0.172	0.445	0.934
HTT2000	-	20.5	31.9	41.1	0.153	0.408	0.935
HTT2300	-	19.6	30.9	40.2	0.102	0.305	0.957
HTT2500	0.342	21.7	31.5	42.6	0.040	0.199	0.958
HTT2800	0.339	14.6	29.8	40.4	0.038	0.170	0.976

[a] d_{002} is interlayer spacing from X-ray diffraction patterns.

[b] HWHM is the half width at half-maximum intensity.

[c] $I_{D'}/I_G$ is the intensity of the D' band over the intensity of the G band.

[d] I_D/I_G is the intensity of the D band over the intensity of the G band.

[e] $I_{G'}/I_G$ is the intensity of the G' band over the intensity of the G band.

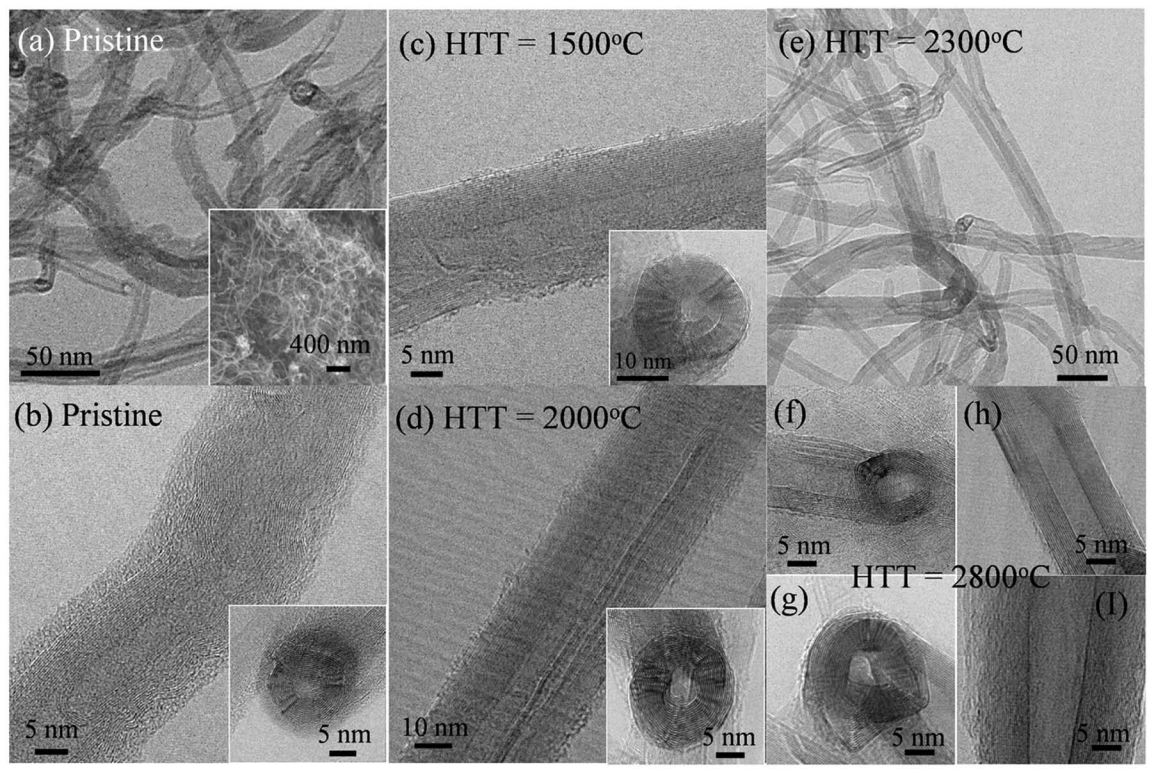
(a) Pristine
50 nm
400 nm
(c) HTT = 1500°C
5 nm
10 nm
(e) HTT = 2300°C
50 nm
(b) Pristine
5 nm
5 nm
(d) HTT = 2000°C
10 nm
5 nm
(f)
5 nm
(h)
5 nm
HTT = 2800°C
(g)
5 nm
(I)
5 nm

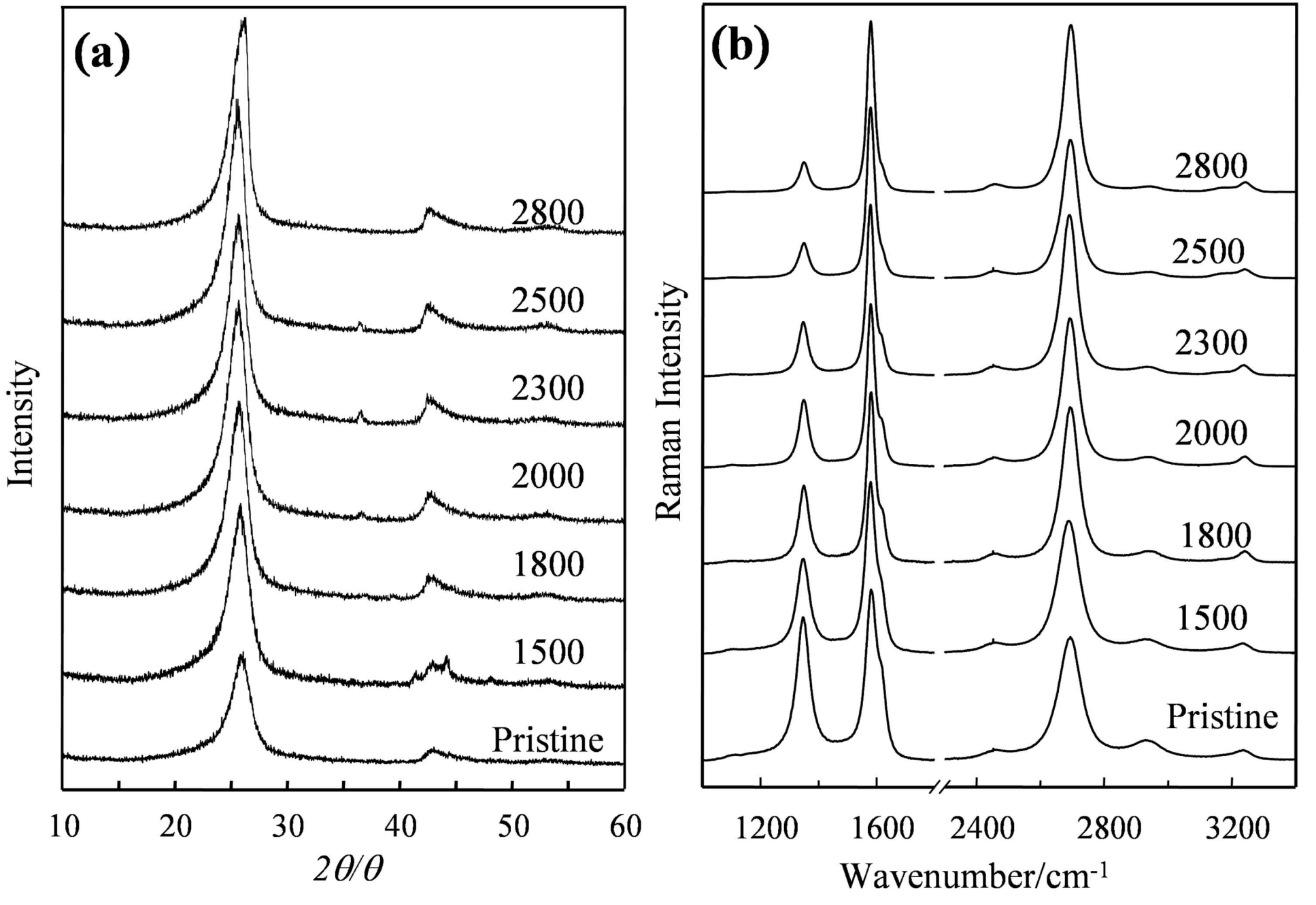
(a)
Intensity
2800
2500
2300
2000
1800
1500
Pristine
10
20
30
40
50
60
2θ/θ
(b)
Raman Intensity
2800
2500
2300
2000
1800
1500
Pristine
1200
1600
2400
2800
3200
Wavenumber/cm-1

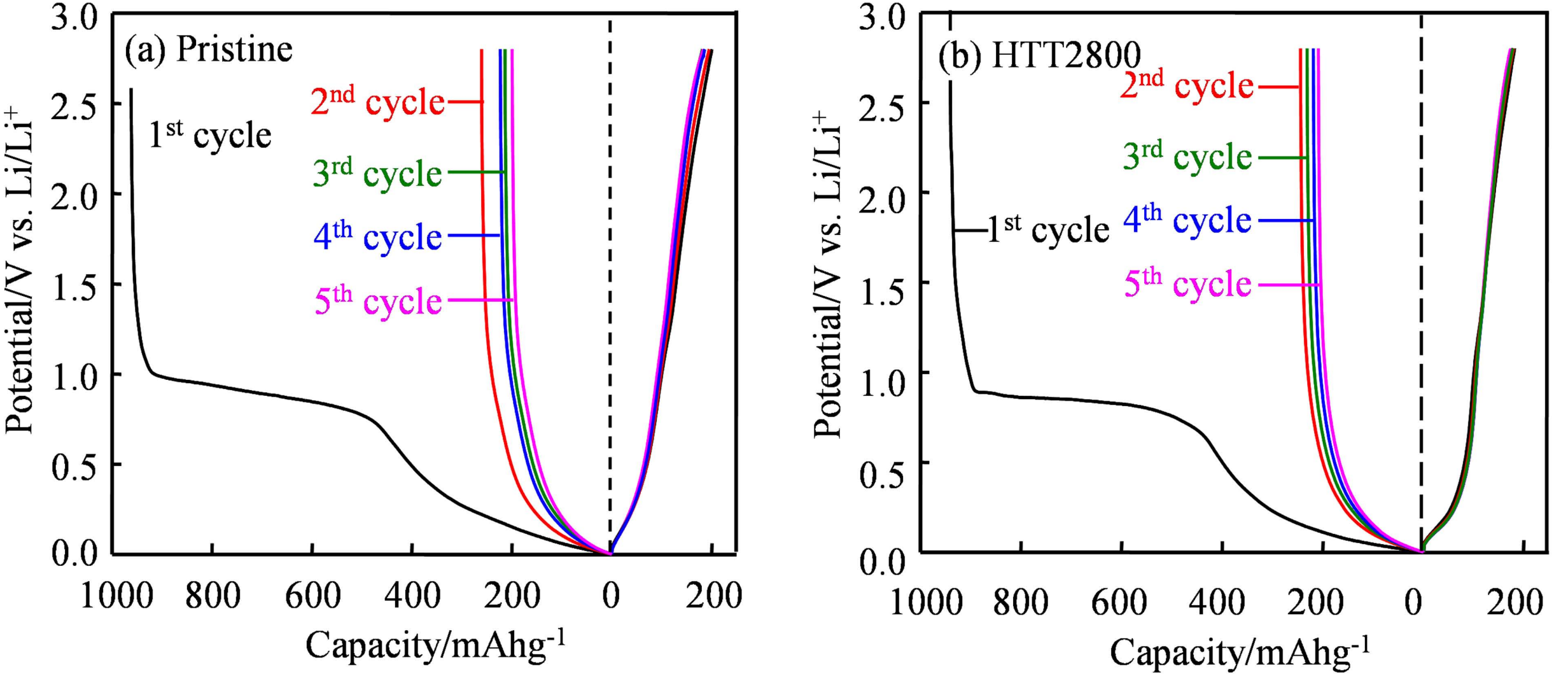
(a) Pristine
1st cycle
2nd cycle
3rd cycle
4th cycle
5th cycle
Potential/V vs. Li/Li+
Capacity/mAhg-1
3.0
2.5
2.0
1.5
1.0
0.5
0.0
1000
800
600
400
200
0
200
(b) HTT2800
1st cycle
2nd cycle
3rd cycle
4th cycle
5th cycle
Potential/V vs. Li/Li+
Capacity/mAhg-1

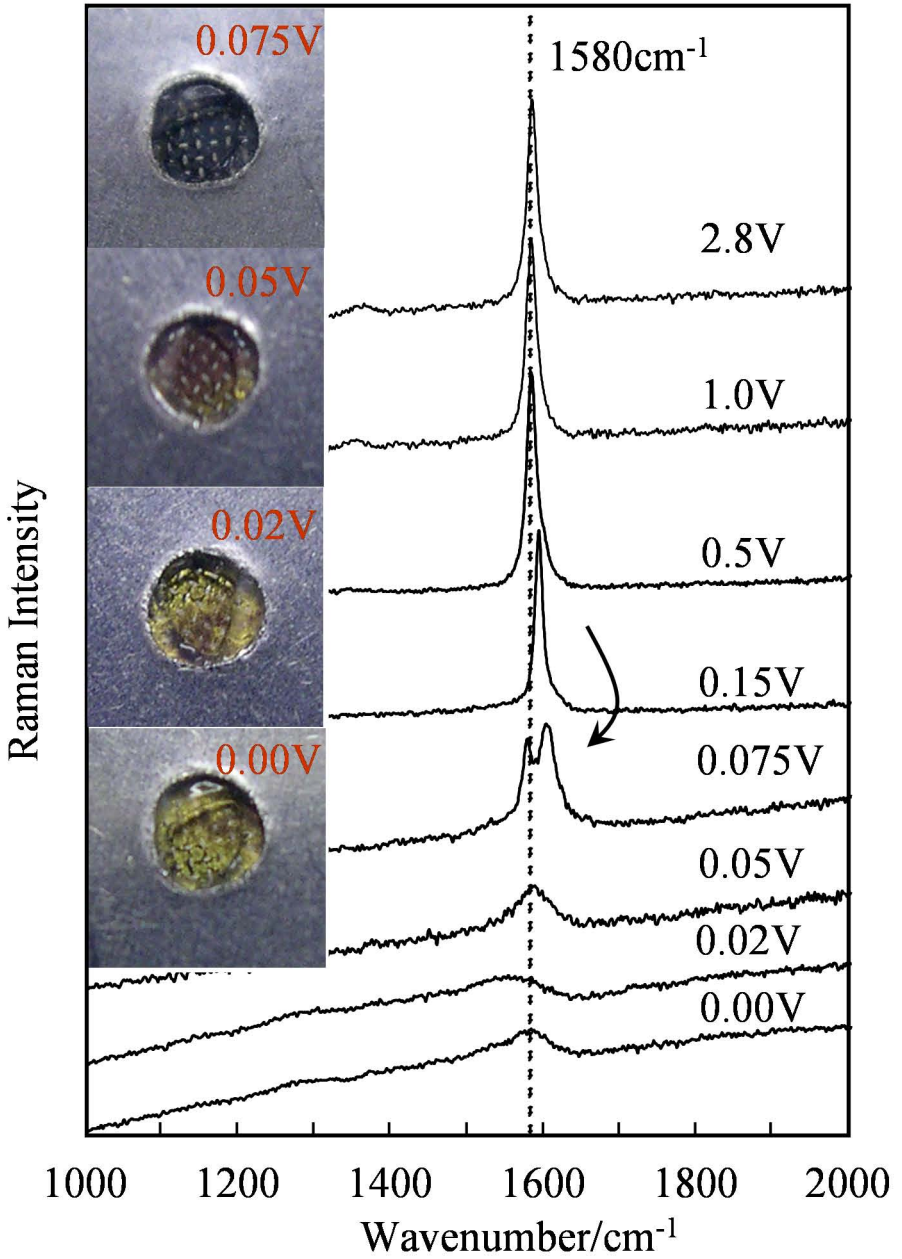
0.075V
0.05V
0.02V
0.00V
1580cm-1
2.8V
1.0V
0.5V
0.15V
0.075V
0.05V
0.02V
0.00V
Raman Intensity
1000
1200
1400
1600
1800
2000
Wavenumber/cm-1

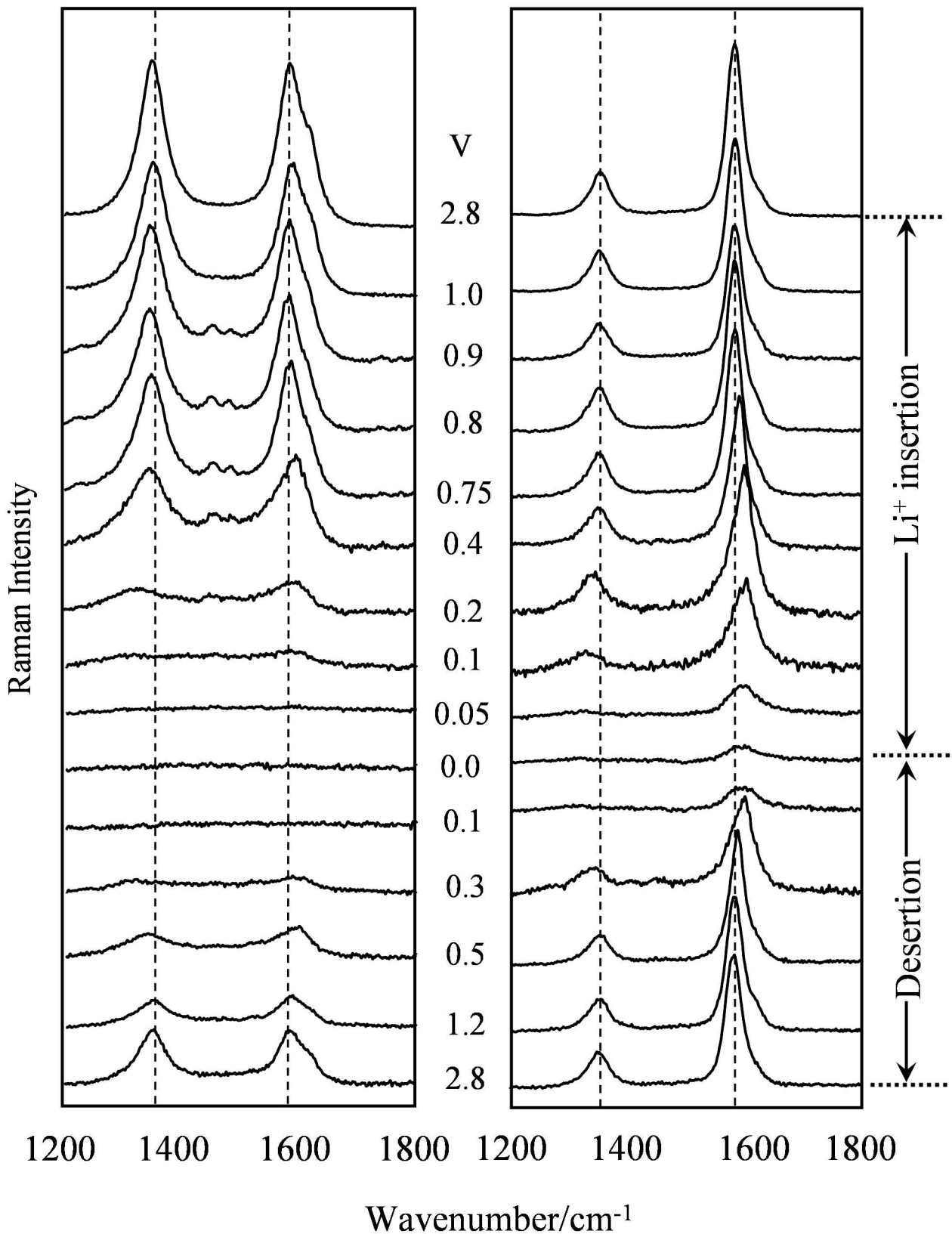
(a) Pristine
(b) HTT2800
V
2.8
1.0
0.9
0.8
0.75
0.4
0.2
0.1
0.05
0.0
0.1
0.3
0.5
1.2
2.8
Li+ insertion
Desertion
Raman Intensity
1200
1400
1600
1800
1200
1400
1600
1800
Wavenumber/cm-1